

The luminosity and stellar mass Fundamental Plane of early-type galaxies

Joseph B. Hyde & Mariangela Bernardi*

Department of Physics & Astronomy, University of Pennsylvania, 209 S. 33rd St., Philadelphia, PA 19104, USA

11 October 2021

ABSTRACT

From a sample of $\sim 50,000$ early-type galaxies from the Sloan Digital Sky Survey (SDSS), we measured the traditional Fundamental Plane in the g , r , i and z bands. We then replaced luminosity with stellar mass, and measured the “stellar mass” Fundamental Plane. The Fundamental Plane, $R \propto \sigma^a / I^B$, steepens slightly as one moves from shorter to longer wavelengths: the orthogonal fit has slope $a = 1.40$ in the g band and 1.47 in z , with a statistical random error of ~ 0.02 . However, systematic effects can produce larger uncertainties, of order ~ 0.05 . The Fundamental Plane is thinner at longer wavelengths: it has an intrinsic scatter of 0.062 dex in g and 0.054 dex in z . We have clear evidence that the scatter is larger at small galaxy sizes/masses; at large masses measurement errors account for essentially all of the observed scatter (about 0.04 dex), suggesting that the Plane is rather thin for the very massive galaxies. The Fundamental Plane steepens further when luminosity is replaced with stellar mass, to 1.54 or 1.63 when stellar masses are estimated from broad-band colors or from spectra, respectively. The intrinsic scatter also reduces further, to 0.048 dex on average. Since color and stellar mass-to-light ratio are closely related, this explains why color can be thought of as the fourth Fundamental Plane parameter. However, the slope of the stellar mass Fundamental Plane remains shallower than the value of 2 associated with the virial theorem. This is because the ratio of dynamical to stellar mass increases at large masses: $M_{\text{dyn}}/M_* \propto M_{\text{dyn}}^{0.17 \pm 0.01}$. This scaling is the edge-on projection of the stellar mass κ -space. The face-on view suggests that there is an upper limit to the stellar density for a given dynamical mass, and this decreases at large masses: $M_*/R_e^3 \propto M_{\text{dyn}}^{-4/3}$. All these trends can be used to constrain early-type galaxy formation models.

We also study how the estimated coefficients a and B of the Plane are affected by other selection effects, whether in apparent or absolute quantities. For example, if low luminosity objects are missing from the sample, and one does not account for this, then a and B are both biased low from their true values. If objects with small velocity dispersions are missing, then a is biased high, although this matters more for the orthogonal than the direct-fitted quantities. These biases are seen in Fundamental Planes which have no intrinsic curvature, so the observation that a and B scale with L and σ is not, by itself, evidence that the Plane is warped. On the other hand, we show that the Plane appears to curve sharply downwards at the small-size/mass end, and more gradually downwards as one moves towards larger sizes/masses. Whereas the drop at small sizes is real, most of the latter effect is due to correlated errors.

Key words: methods: analytical - galaxies: formation - galaxies: haloes - dark matter - large scale structure of the universe

1 INTRODUCTION

The Fundamental Plane has been a useful diagnostic of galaxy distances and galaxy evolution (e.g. Dressler et al. 1987; Djorgovski & Davis 1987; Jørgensen et al. 1996; Pahre et al. 1998; Bernardi et al. 2003; Jørgensen et al. 2007). If galaxies are virialized, then one expects observable signatures of the balance between potential and kinetic energies.

* E-mail: jhyde,bernardm@physics.upenn.edu

For example,

$$\sigma^2 \propto \frac{GM_{dyn}}{R} \propto \frac{M_{dyn}}{L} \frac{L}{R^2} R \propto \frac{M_{dyn}}{L} I R, \quad (1)$$

where σ is a velocity dispersion, I is a surface brightness, R is a scale, and M_{dyn}/L is the mass to light ratio. This suggests that the observed line-of-sight velocity dispersion σ_e^2 and surface brightness $I_e \equiv L/(2\pi R_e^2)$ at or within some fiducial radius R_e should be correlated with one another. (In what follows, we will use the subscript e to denote quantities estimated from deVaucouleur's (1948) fits to the surface brightness profiles.)

Velocity dispersion and surface brightness are distance-independent observables, whereas the size is not, so it is common to write

$$R_e \propto \sigma_e^a I_e^{-B}, \quad (2)$$

and to find that pair (a, B) for which the scatter either in the R_e direction, or in the direction orthogonal to the Plane, is minimized. If the resulting values of (a, B) differ from the virial scalings $(2, 1)$, then the Fundamental Plane is said to be 'tilted'. The tilt of the Fundamental Plane is interpreted as evidence that the mass-to-light ratio (M_{dyn}/L) depends on some combination of the observables (R_e, I_e, σ_e) – the prejudice that galaxies are virialized sets what this combination must be: $(M_{dyn}/L) \propto \sigma_e^{2-a} I_e^{B-1}$. In low redshift ($z \sim 0.1$) samples, $a \sim 1.5$ and $B \sim 0.8$, so the implied M_{dyn}/L is expected to increase slightly with M_{dyn} or L . Jørgensen et al. (2007) find that $a = 0.6$, $B = 0.7$ and $M_{dyn}/L \propto M^{0.54}$ at $z \sim 0.9$.

Contributions to the tilt of the Fundamental Plane can be further examined by expressing the mass-to-light ratio in terms of the dynamical mass, total mass, stellar mass, and broadband luminosity:

$$\left(\frac{M_{dyn}}{L}\right) = \left(\frac{M_{dyn}}{M_{tot}}\right) \left(\frac{M_{tot}}{M_*}\right) \left(\frac{M_*}{L}\right) \quad (3)$$

where M_{tot} is the sum of dark matter and baryonic mass, M_* is the stellar mass, and L is the observed broadband luminosity. If any of these terms varies as a function of M_{dyn} or L , the Plane will be tilted.

The assumption that M_{dyn}/M_{tot} is constant is the assumption of homology. The validity of this assumption is supported by detailed kinematic modeling of galaxies observed with SAURON integral-field spectroscopy. The combination of 2-D photometric and spectroscopic data allowed Cappellari et al. (2007) to account for differences in e.g. $\rho(r)$, $\sigma(r)$, and $V(r)$. They found that dynamical mass is a robust tracer of total mass. More recent work by Bolton et al. (2008) suggests that the deVaucouleur-based quantity $R_e \sigma_e^2$ is linearly proportional to the mass estimated from the strong gravitational lensing effect, further reinforcing the homology assumption that $M_{dyn} \propto M_{tot}$.

For a given IMF, the stellar mass to light ratio, (M_*/L) , depends on the age and metallicity of the stellar population as well as on wavelength (e. g., Tinsley 1978; Worthey 1994). There is now growing evidence for correlations between mass and metallicity (e.g., Trager et al. 2000; Nelan et al. 2005; Thomas et al. 2005), and between age and velocity dispersion (e.g., Bernardi et al. 2005). Hence, stellar population models predict that (M_*/L) will depend on total mass and luminosity, plausibly producing a tilt that will depend on

waveband. While there is evidence that the tilt does indeed depend on waveband, the dependence is weak (Pahre et al. 1998; Bernardi et al. 2003; La Barbera et al. 2008), and so this effect alone cannot explain all of the tilt.

There is little discussion in the literature of the possibility that the IMF changes along the sequence in such a way as to make the dependence on M_*/L weak. If there is no such effect, then stellar population effects and non-homology are weak, so the dominating contribution to the tilt of the Fundamental Plane is due to the systematic variation of M_{tot}/M_* with mass. In a hierarchical scenario of galaxy formation, the relative distribution of stars and dark matter in a galaxy depend on the roles of dissipational and dissipationless merging (e.g. Bender et al. 1992). Hydrodynamical simulations of galaxy mergers (Robertson et al. 2006; Hopkins et al. 2008) suggest that the fractional gas content of merging galaxies determines the fundamental Plane of their remnants. Further dissipationless mergers preserve the Fundamental Plane, but not its projections (e.g., Boylan-Kolchin et al. 2005). Observations of brightest cluster galaxies by Bernardi et al. (2007) support these conclusions.

The dissipational content in mergers sets the effective mass-to-light ratio of the merger remnant (Robertson et al. 2006; Hopkins et al. 2008). If the dissipational content varies with mass (in spirals the gas fraction decreases with mass, e.g. Bell & deJong 2000), this would cause a systematic dependence of the mass-to-light ratio with mass. If this ratio varies as a power law with mass ($M/L \propto M^\alpha$), then the Fundamental Plane would be tilted relative to the virial scaling. If the mass-to-light ratio varies in a more complicated manner, the Fundamental Plane could be warped, or have a more complicated shape.

Therefore, in the present work, we separate out the contribution from these effects by re-writing equation (1) as:

$$\sigma^2 \propto \left(\frac{M_{dyn}}{M_*}\right) \left(\frac{M_*}{L}\right) \left(\frac{L}{R^2}\right) R. \quad (4)$$

We do not consider variation of (M_{dyn}/M_{tot}) , since two rather different methods (Cappellari et al. 2007; Bolton et al. 2008) suggest that this ratio is a constant across the early-type population. (This is also why we do not include effects associated with fitting Sersic's 1968 generalization of the deVaucouleur profile to the images, even though there is a well-developed literature on this subject.) If the stellar population models which one uses to estimate M_*/L are accurate, then multiplying the surface brightness by M_*/L should eliminate most of the dependence on waveband. (There is a small remaining dependence which arises from the fact that the half-light radii are slightly but systematically smaller in redder bands, e.g. Hyde & Bernardi 2009). The remaining term (M_{dyn}/M_*) is the ratio of the dynamical to stellar mass, which we will use as our proxy for structural differences. This is interesting because M_{dyn}/M_* is not expected to be very much greater than unity – recent work suggests that $M_{dyn}/M_* \approx 1/0.7$ (Cappellari et al. 2007) – how it scales with mass is a quantity of great interest to galaxy formation models (e.g. Bower et al. 2006; DeLucia et al. 2006; Hopkins et al. 2008), and previous work in the SDSS suggests that M_{dyn}/M_* is not constant across the early-type population (Padmanabhan et al. 2004; Gallazzi et al. 2006)

Section 2 discusses how we select our sample and shows the result of fitting for the coefficients (a, B) of the tradi-

tional Fundamental Plane in the SDSS g , r , i , and z bands. (Appendix A shows that our sample probably contains some non-early-type galaxies but they are too few to affect our conclusions.) We also study the possibility of detecting if the Plane is warped, or merely thick. This is prompted in part by recent work showing that the parameters of the fitted Fundamental Plane appear to depend on the luminosity and velocity dispersion range of the sample (D’Onofrio et al. 2008; Nigoche-Netro et al. 2009). We show that such dependences exist in thick Planes that are not warped – they are a consequence of not accounting for selection effects. We then discuss more reliable estimates of curvature along the Plane.

Section 3 describes our estimates of M_*/L and the result of fitting for the coefficients (α, β) in

$$R_e \propto \sigma_e^\alpha \Sigma_e^{-\beta} \quad (5)$$

where $\Sigma \equiv (M_*/L)I$. The difference between (α, β) and (a, b) is due to stellar population effects; the difference between (α, β) and the virial scalings $(2, 1)$ encodes information about M_{dyn}/M_* . If $(\alpha, \beta) < (2, 1)$ then (M_{dyn}/M_*) increases with M_{dyn} or M_* for the same reason that $(a, b) < (2, 1)$ implies (M_{dyn}/L) increases with M_{dyn} or L .

A complementary analysis of the Fundamental Plane variables was introduced by Bender, Burstein & Faber (1992). This construction, which they termed κ -space, was criticized as being an “obfuscation, not a simplification”, by Pahre et al. (1998), primarily on the grounds that R_e and I_e depend on waveband. However, by replacing luminosity with stellar mass, what we will call κ_* -space, most of the wavelength dependence is removed; only the weak dependence of R_e on waveband remains. So it is interesting to examine how early-types are distributed in κ_* -space. Section 4 presents the first analysis of κ_* -space. The scaling of M_*/M_{dyn} with M_{dyn} referred above is the edge-on view of the κ_* -Plane. The face-on view provides a relation between the maximum stellar density and dynamical mass of early-type galaxies.

A final section summarizes our findings and discusses some implications.

2 FP: THE TRADITIONAL FUNDAMENTAL PLANE

We use the sample of about 50,000 early-type galaxies assembled by Hyde & Bernardi (2008). The sample is based on the SDSS-DR4, but with photometric and spectroscopic parameters updated from the SDSS-DR6 database. Briefly, objects have deVaucouleur magnitudes $14.5 < m_r < 17.5$, $\text{fracDev} = 1$ in both the g - and r -bands, and axis ratios $b/a \geq 0.6$. Appendix A shows that these cuts almost certainly do not yield a pure early-type galaxy sample (e.g., the face-on analogues of the objects with $\text{fracDev}=1$ and $b/a \leq 0.6$ are still in our sample). However, the non-early types in our sample are too few to affect our conclusions.

Photometric parameters for the best-fit deVaucouleur surface brightness profiles are “corrected” for known problems which arise from the SDSS sky-subtraction algorithm. In addition, there are some systematic differences between the velocity dispersions output by SDSS-DR6 and the

IDLspec2d reduction (Hyde & Bernardi 2009). Our velocity dispersion estimates are simply the average of the two reductions (Section 2.1.2 discusses the dependence of the Fundamental Plane parameters on systematics). We also compute the velocity dispersion for objects for which the SDSS pipeline does not estimate σ (due to low S/N or the presence of weak emission lines, i.e. the **status** flag not-equal to 4). We select galaxies with velocity dispersions $60 < \sigma < 400 \text{ km s}^{-1}$. The velocity dispersions are then corrected to $R_e/8$. Stellar mass estimates, from Gallazzi et al. (2005), are available for all these objects. Since these are actually stellar mass to light ratios multiplied by a luminosity, and we have corrected the luminosities for the sky-subtraction problems whereas Gallazzi et al. did not, we apply a correction to their stellar masses to account for this effect. Where necessary, distances were computed from redshifts assuming a Hubble constant of $70 \text{ km s}^{-1} \text{ Mpc}^{-1}$ in a flat Λ CDM model with $\Omega_0 = 0.3$.

2.1 Fitting the Plane

We fit the Plane as follows. We begin by writing the Fundamental Plane as

$$\log_{10} \left(\frac{R_e}{\text{kpc}} \right) = a \log_{10} \left(\frac{\sigma}{\text{km s}^{-1}} \right) + b \frac{\mu_e}{\text{mags}} + c, \quad (6)$$

where $c = \langle \log_{10} R \rangle - a \langle \log_{10} \sigma \rangle - b \langle \mu_e \rangle$, and μ_e is the mean surface brightness within the half light radius, defined explicitly as follows:

$$\begin{aligned} \mu_e &= -2.5 \log_{10}(I_e) = -2.5 \log_{10} \left(\frac{L}{2\pi R_e^2} \right) \\ &= m + 5 \log_{10}(r_e) + 2.5 \log_{10}(2\pi) - 10 \log_{10}(1+z) \end{aligned} \quad (7)$$

where m is the evolution, reddening, and k -corrected apparent magnitude (refer to Hyde & Bernardi 2009 for details on magnitudes), and r_e is the angular size in arcseconds. In this form, the virial scaling would follow $(a, b) = (2, 0.4)$ because of the -2.5 term in the definition of μ_e . Unless we say so explicitly, we work in logarithmic units. Therefore, following Bernardi et al. (2003), we will sometimes abuse notation by using R to denote $\log_{10}(R_e/\text{kpc})$, V to denote $\log_{10}(\sigma/\text{km s}^{-1})$, and I to denote μ_e . Thus, for example, e_R, e_V and e_I denote the measurement errors on $\log R_e$, $\log \sigma$, and μ_e .

The shape of the Fundamental Plane is determined by estimating a and b . This is done either by minimizing residuals in the R_e direction, or in the direction orthogonal to the fit. In general the ‘direct’ and ‘orthogonal’ fit parameters are different combinations of the mean values of and covariances between the variables $\log_{10} R$, $\log_{10} \sigma$ and μ_e .

In practice, naive estimation of these means and covariances (e.g. simply summing over the data without including other weight terms) may lead to biases induced by measurement errors (these usually affect the covariances) or by selection effects (which bias the means and the covariances). The effects of both must be accounted-for to estimate the intrinsic shape parameters a and b (e.g. Saglia et al. 2001). This is especially important when the FP is determined for galaxies in a magnitude limited sample (Bernardi et al. 2003). We do this following methods described in Sheth & Bernardi (2009). Analytic expressions which quantify the bias in the

Fundamental Plane due to the magnitude limit of the survey may be found there.

Briefly, the effect of the magnitude limit is removed by weighting each object by $V_{\max}^{-1}(L)$, the inverse of the volume over which it could have been observed, and measurement errors are subtracted in quadrature from the measured covariances. The mean values of magnitude, size, surface-brightness, and velocity dispersion in the r -band are

$$\begin{aligned} \langle M_r / \text{mags} \rangle &= -20.99, & \langle \log R_e / \text{kpc} \rangle &= 0.39, \\ \langle \mu_e \rangle &= 19.53, & \langle \log \sigma / \text{km s}^{-1} \rangle &= 2.19. \end{aligned} \quad (8)$$

With typical measurement errors

$$\begin{aligned} \mathcal{E} &= \begin{pmatrix} \langle e_I^2 \rangle & \langle e_I e_R \rangle & \langle e_I e_V \rangle \\ \langle e_I e_R \rangle & \langle e_R^2 \rangle & \langle e_R e_V \rangle \\ \langle e_I e_V \rangle & \langle e_R e_V \rangle & \langle e_V^2 \rangle \end{pmatrix} \\ &= \begin{pmatrix} 0.0542 & 0.0162 & 0 \\ 0.0162 & 0.0049 & 0 \\ 0 & 0 & 0.0016 \end{pmatrix} \end{aligned} \quad (9)$$

we find that the intrinsic covariance matrix (i.e. corrected for measurement errors and the magnitude limited selection effect) is

$$\begin{aligned} \mathcal{F} &= \begin{pmatrix} C_{II} & C_{IR} & C_{IV} \\ C_{IR} & C_{RR} & C_{RV} \\ C_{IV} & C_{RV} & C_{VV} \end{pmatrix} \\ &= \begin{pmatrix} 0.2947 & 0.0782 & -0.0096 \\ 0.0782 & 0.0552 & 0.0189 \\ -0.0096 & 0.0204 & 0.0187 \end{pmatrix}. \end{aligned} \quad (10)$$

From this covariance matrix we obtain

$$a_{\text{dir}} = 1.170 \quad \text{and} \quad b_{\text{dir}} = 0.303 \quad (11)$$

$$a_{\text{ort}} = 1.434 \quad \text{and} \quad b_{\text{ort}} = 0.315. \quad (12)$$

The observed rms scatter about the direct fit is 0.107, of which 0.096 is intrinsic. These quantities for the orthogonal fit are 0.066 and 0.058 respectively. The uncertainty on the coefficients a and b is dominated by systematic effects more than random errors, as described here below. Typical uncertainties on the coefficients due to random errors are $\delta a < 0.02$ and $\delta b < 0.01$. Systematics errors give $\delta a \sim 0.05$ and $\delta b \sim 0.02$.

2.1.1 Dependence of δa and δb on sample size

We analyze how the uncertainty on a and b depend on sample size using bootstrap resampling. Figures 1 and 2 show how δa and δb depend on sample size. They were obtained by dividing the total sample up into smaller subsamples, each containing N_{gal} galaxies. For a given N_{gal} , we do not include any galaxy more than once, so there are a total of $N = N_{\text{tot}}/N_{\text{gal}}$ subsamples. We then fit the FP in each subsample, and computed the mean and rms values of a , b and intrinsic scatter. Figure 1 shows that the precision increases as the number of objects in the sample increases, as one might expect. However, Figure 2 shows that sample sizes smaller than about 300 tend to result in underestimates of the intrinsic scatter, in good agreement with La Barbera et al. (2000). For a sample of $\sim 50,000$ galaxies the statistical random error δa and δb are quite small: $\delta a < 0.02$ and $\delta b < 0.01$.

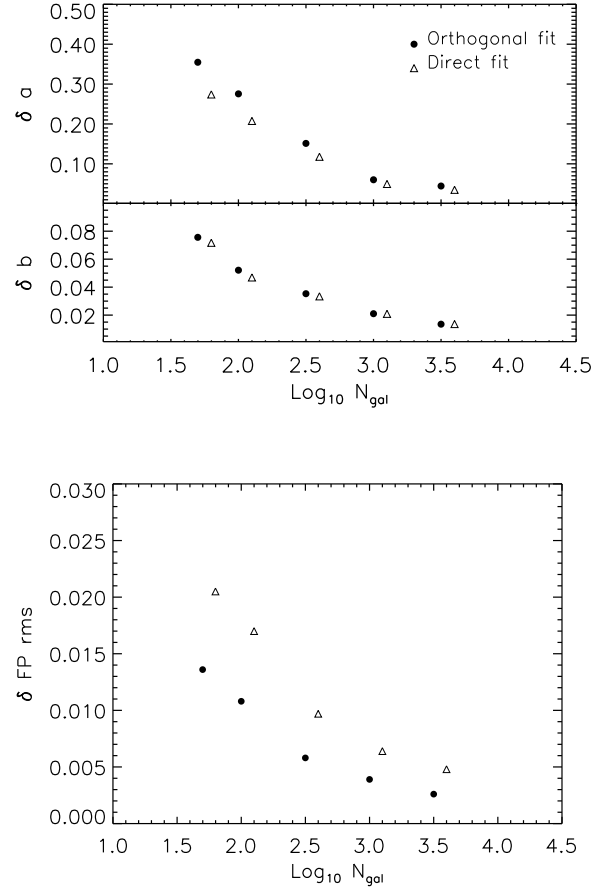


Figure 1. Precision of the FP coefficients a , b and scatter as the number of galaxies used to fit the FP changes. The quantities δa , δb and $\delta \text{FP rms}$ show the standard deviation values of a , b and the scatter around the FP, obtained from fitting the FP to $N = N_{\text{tot}}/N_{\text{gal}}$ subsamples of the whole sample (i.e. each galaxy was chosen only once). Triangles and circles show results for the direct and orthogonal fits, respectively. For clarity, the triangles have been slightly shifted to the right.

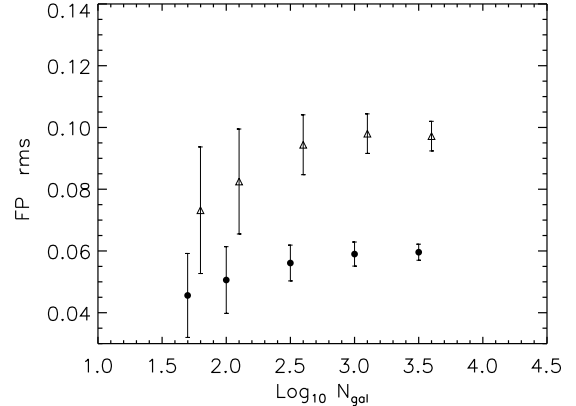


Figure 2. As for Figure 1, but now for the dependence of the estimated intrinsic scatter around the FP on sample size. Error bars show the $\delta \text{FP rms}$ values from Figure 1.

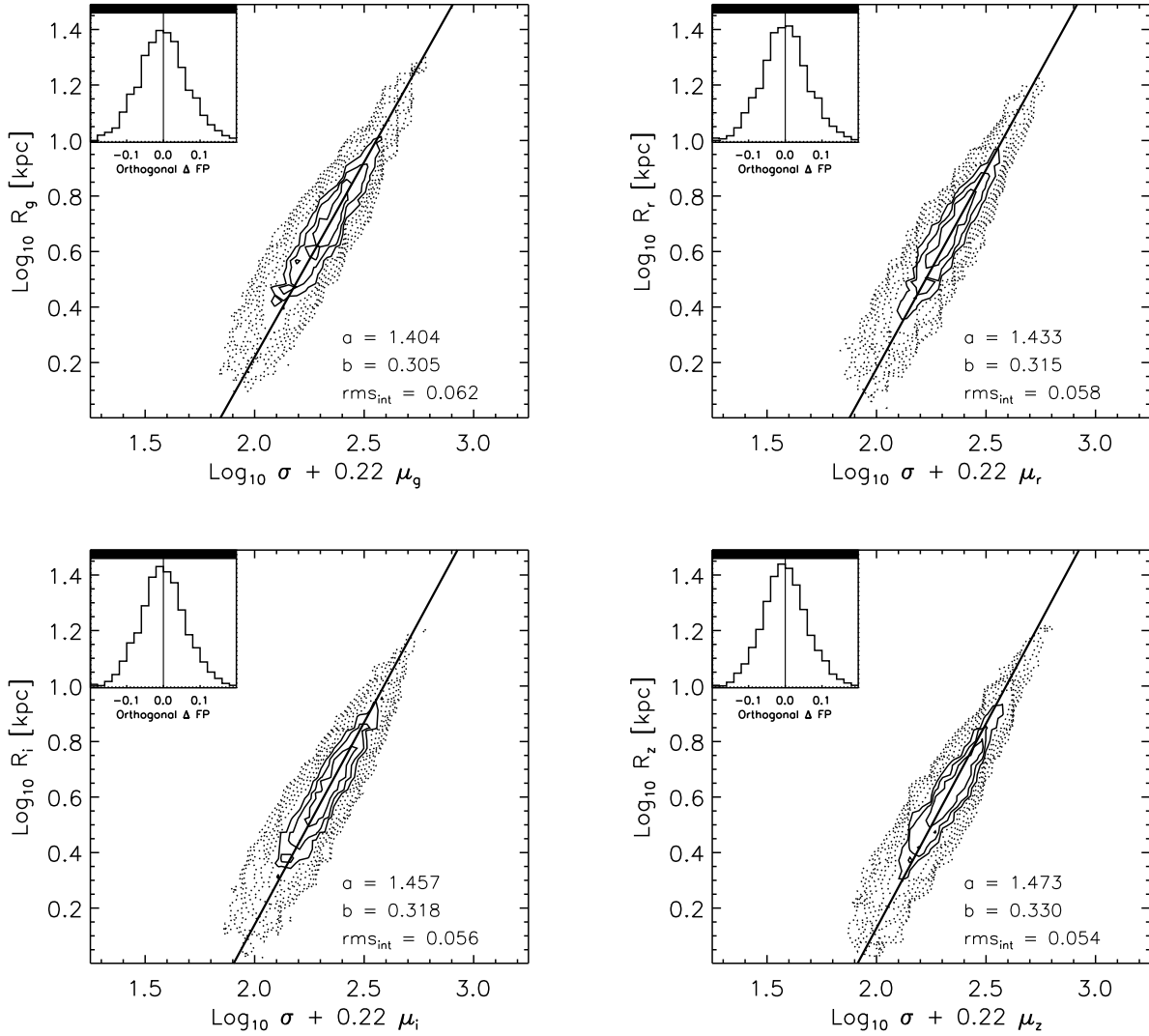


Figure 3. The Fundamental Plane in the g , r , i and z bands. Typical uncertainties on the coefficients due to random errors are $\delta a \sim 0.02$ and $\delta b \sim 0.01$. Systematics errors give $\delta a \sim 0.05$ and $\delta b \sim 0.02$.

2.1.2 Dependence of δa and δb on systematics

When working with a large galaxy sample, systematic effects may be more important than random errors. The correction applied to the magnitudes, sizes and stellar masses for known problems which arise from the SDSS sky-subtraction algorithm (Hyde & Bernardi 2009), results in small changes to a and b – the variation is less than 0.01 for both coefficients.

However, recall that our estimate of the velocity dispersion is the average of the DR6 and IDLSpec2d values. If we only use the DR6 values, we find $(a_{\text{direct-DR6}}, b_{\text{direct-DR6}}) = (1.189, 0.303)$ with intrinsic scatter 0.108 dex, and $(a_{\text{orth-DR6}}, b_{\text{orth-DR6}}) = (1.464, 0.315)$ with scatter 0.058 dex. Using the IDLSpec2d reductions instead gives $(a_{\text{direct-IDLSpec2d}}, b_{\text{direct-IDLSpec2d}}) = (1.122, 0.304)$, with intrinsic scatter 0.100 dex, and $(a_{\text{orth-IDLSpec2d}}, b_{\text{orth-IDLSpec2d}}) = (1.401, 0.317)$ with scatter 0.061 dex, respectively. This suggests that we should

assume as typical systematic error $\delta a \sim 0.05$ and $\delta b \sim 0.02$. These values are larger than the random errors quoted above, showing that it is important to separate random from systematic errors.

2.2 Dependence on selection

If we do not account for selection effects we find mean values $\langle M_r \rangle = -21.94$, $\langle \log R_e \rangle = 0.62$, $\langle \mu_e \rangle = 19.71$ and $\langle \log \sigma \rangle = 2.30$, and covariances $C_{II} = 0.2660$, $C_{RR} = 0.0488$, $C_{VV} = 0.0127$, $C_{IR} = 0.0820$, $C_{IV} = 0.0036$ and $C_{RV} = 0.0159$. Although these covariances have changed, the coefficients of the Fundamental Plane change little: $(a_{\text{direct}}, b_{\text{direct}}) = (1.1723, 0.2924)$ with intrinsic scatter 0.079, and $(a_{\text{orth}}, b_{\text{orth}}) = (1.4235, 0.2914)$ with scatter 0.047. Note that the intrinsic scatter is smaller! This is largely because the distribution of luminosities in a magnitude limited survey is narrower than in a volume limited survey (because the faint objects are under-represented); if

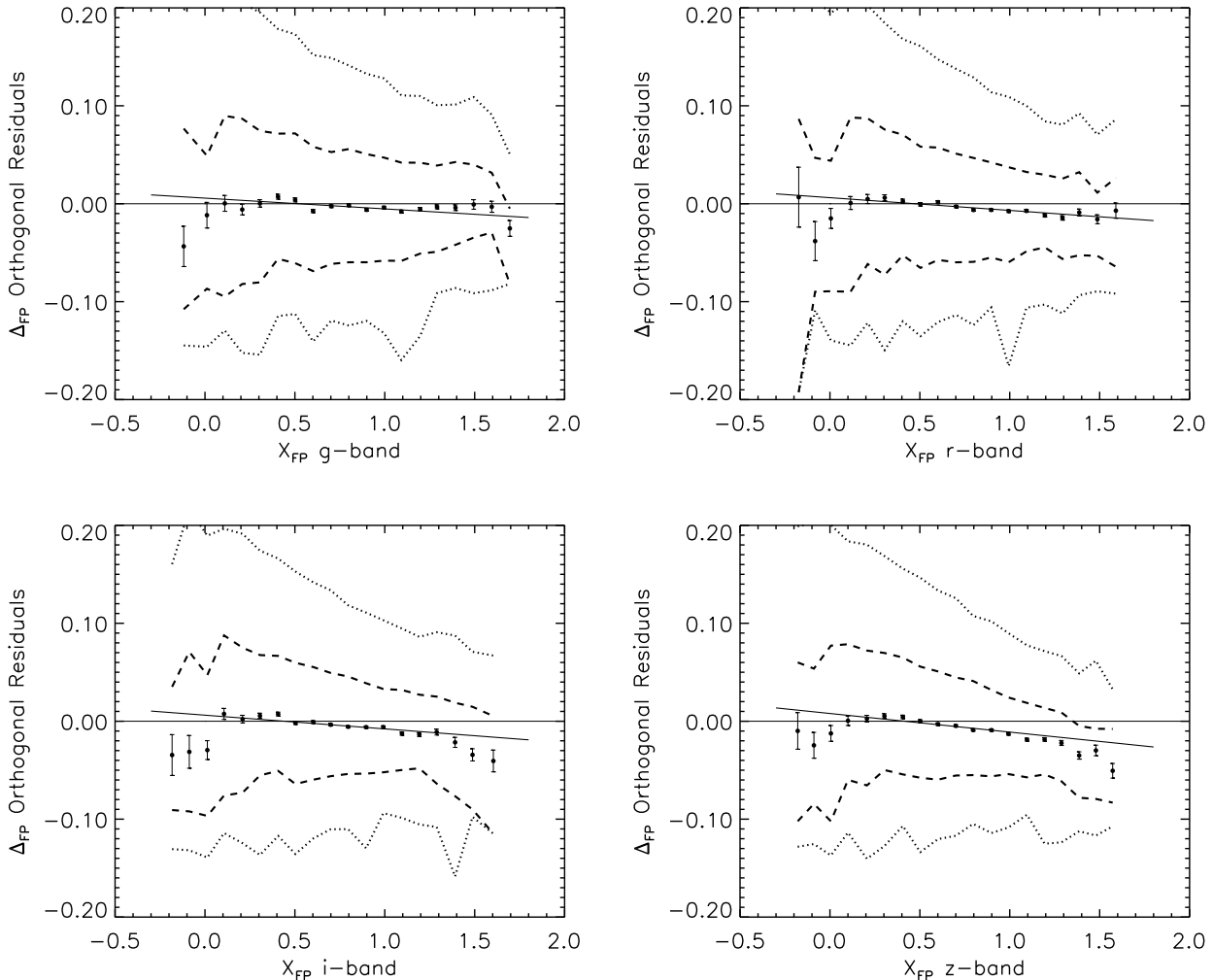


Figure 4. Fundamental Plane residuals with respect to the orthogonal fit in the g , r , i and z bands, shown as a function of distance X_{FP} along the Plane. Symbols show the median residual in narrow bins in X_{FP} ; dashed and dotted lines enclose 68% and 95% of the points. Solid lines show the expected trend due to correlated measurement errors.

one does not account for this, then the magnitude limited catalog is more homogeneous, making for a tighter FP. The fact that the coefficients a and b hardly change is largely fortuitous (Sheth & Bernardi 2009 show why they are expected to change); it happens because the scaling relations are actually slightly curved (see Section 2.4, and also Hyde & Bernardi 2009).

Had we not removed objects with $b/a < 0.6$ then $C_{II} = 0.3756$, $C_{RR} = 0.0549$, $C_{VV} = 0.0171$, $C_{IR} = 0.0948$, $C_{IV} = -0.0132$ and $C_{RV} = 0.0171$. The resulting FP has $(a_{\text{direct}}, b_{\text{direct}}) = (1.1674, 0.2936)$ with intrinsic scatter 0.091, and $(a_{\text{orth}}, b_{\text{orth}}) = (1.4294, 0.3052)$ with scatter 0.055. Since objects with $b/a < 0.6$ are almost certainly not early-types, the fact that a and b are almost the same as when these objects have been removed suggests that the presence of a few non-early-types in our sample has little effect on our findings.

Finally, selecting only galaxies with SDSS-DR6 velocity dispersions (i.e. excluding objects with low S/N spectra or presence of weak emission lines, i.e. the `status` flag not-

equal to 4) changes a and b very slightly – the variation is less than 0.01 for both coefficients. Table 1 compares the r -band FP coefficients associated with these various selection and parameter choices.

2.3 Dependence on waveband

The Fundamental Planes associated with the orthogonal fits to the g , r , i and z band data are shown in Figure 3. The coefficients (a, b) of these Fundamental Planes are shown in each panel; they are also reported in Table 2, as are the corresponding coefficients of the direct fits. Notice that there is a small but systematic increase of a with wavelength. To estimate its significance, we require an estimate of the errors on a and b . Although systematics associated with how σ was measured make $\delta a \sim 0.05$, $\delta b \sim 0.02$, this additional systematic error is not relevant if we wish to compare the Planes at different wavelengths, because the same choice for σ is made for all wavelengths. What matters here is the typical uncertainty due to random errors on these best fit values.

Table 1. Dependence of r -band Fundamental Plane coefficients on sample selection and parameters. Typical uncertainties on the coefficients due to random errors are $\delta a \sim 0.02$ and $\delta b \sim 0.01$; sytematics are $\delta a \sim 0.05$ and $\delta b \sim 0.02$.

Band	a	b	rms_{int}
direct			
r	1.1701	0.3029	0.0964
DR6- σ	1.1892	0.3032	0.1081
spec2d- σ	1.1223	0.3041	0.1002
no-Vmax	1.1703	0.3036	0.0792
all b/a	1.1674	0.2936	0.0913
orthog			
r	1.4335	0.3150	0.0578
DR6 σ	1.4642	0.3151	0.0581
spec2d σ	1.4013	0.3173	0.0613
no-Vmax	1.4235	0.2914	0.0473
all b/a	1.4294	0.3052	0.0554

Table 2. Coefficients (a, b) of the Luminosity Fundamental Plane. Typical uncertainties on the coefficients due to random errors are $\delta a \sim 0.02$ and $\delta b \sim 0.01$. Sytematics errors give $\delta a \sim 0.05$ and $\delta b \sim 0.02$.

Band	a	b	c	rms_{obs}	rms_{int}
direct					
g	1.1154	0.2957	-8.0463	0.1102	0.1005
r	1.1701	0.3029	-8.0858	0.1074	0.0964
i	1.1990	0.3036	-8.0481	0.1067	0.0950
z	1.2340	0.3139	-8.2161	0.1052	0.0921
orthog					
g	1.4043	0.3045	-8.8579	0.0696	0.0617
r	1.4335	0.3150	-8.8979	0.0664	0.0578
i	1.4572	0.3182	-8.8914	0.0652	0.0563
z	1.4735	0.3295	-9.0323	0.0635	0.0538

Section 2.1.2 and Figure 1 shows that these random errors are $\delta a \sim 0.02$, $\delta b \sim 0.01$. Thus, we have a 3σ detection of the steepening of the Fundamental Plane with wavelength.

2.4 Evidence for curvature

Figure 4 shows residuals

$$\Delta_{FP} \equiv \frac{\log R_e - a \log \sigma - b \mu_e - c}{\sqrt{1 + a^2 + b^2}} \quad (13)$$

from the orthogonal fit as a function of distance

$$X_{FP} \equiv \frac{a \log R_e + \log \sigma + b \mu_e / a}{\sqrt{1 + a^2}} \quad (14)$$

along the Plane. Weak trends are seen in all bands.

Interpretation of these trends is complicated by the fact that the measurement errors are correlated, and they are larger at small sizes. To see what effect is expected, we must use the numbers from the covariance matrices \mathcal{F} and \mathcal{E} to estimate $\langle \Delta_{FP} X_{FP} \rangle / \langle X_{FP}^2 \rangle$, the expected slope of the correlation shown in Figure 4. In the r -band, $\langle \Delta_{FP} X_{FP} \rangle = 0 - 0.0007$, where the first term is the contribution from \mathcal{F} and the second from \mathcal{E} . I.e., there is no intrinsic correlation (essentially, by definition), but there is a contribution

from the measurement errors. This contribution is easy to estimate because Δ_{FP} is almost proportional to $IP - aV$, where $IP \equiv \log_{10}(R_e) - 0.3\mu_e$, and the error in IP is well-known to be negligible, at least for deVaucouleur-like profiles (Saglia et al. 1997; or see bottom panel of Figure 5 in Hyde & Bernardi 2009), so the error in Δ_{FP} is dominated by the error in V . On the other hand, the error in X_{FP} is due to errors in R, V and IP . Errors in R and V are almost uncorrelated, so the dominant contribution from correlated errors comes from the fact that V appears with different signs in X_{FP} and Δ_{FP} .

A similar analysis of $\langle X_{FP}^2 \rangle$ shows that it is dominated by the contribution from \mathcal{F} rather than \mathcal{E} . In the r -band, $\langle X_{FP}^2 \rangle = 0.087 + 0.008$. Thus, correlated errors are expected to produce a weak trend, with slope -0.007 . The solid line in the Figure shows this trend – it is similar to that observed, suggesting that correlated errors can account for most of the observed weak decline in Δ_{FP} . On the other hand, correlated errors cannot account for the break downwards at small X_{FP} : this is genuine curvature.

A similar analysis in the other bands yields the solid lines shown in Figure 4. This illustrates that sample sizes are now large enough that correlated errors produce systematic effects which must be accounted for when performing the fits.

At the low size/mass end, the Plane is probably warped (Figures 4, and see also Figure 10 below). However, we view this with caution since uncertainties/systematics in the velocity dispersion/size measurements are also larger. The possibility of curvature induced by the presence of spirals in the sample is discussed in Appendix A. We argue that the location of spirals on the fundamental Plane would not result in negative residuals at small X_{FP} , and that the spirals are too few to significantly bias our results.

2.5 Variation in thickness along the Plane

Notice that the Plane is thinner at large X_{FP} . Figure 5 shows that the typical measurement errors vary little with distance along the Plane. Since the observed scatter is larger at smaller X_{FP} (the width of the regions enclosed by the dashed and dotted curves in Figure 4 increases at small X_{FP}), but the contribution from errors is approximately constant, we conclude that the intrinsic scatter around the Plane decreases dramatically as X_{FP} increases. It is remarkable that, at $X_{FP} \gtrsim 1$, measurement errors account for essentially all of the observed scatter (about 0.04 dex), suggesting that the Plane is rather thin at large X_{FP} .

2.6 Potential biases from cuts in L

There has been recent interest in the fact that the coefficients of the FP depend on how the sample was selected, a point emphasized by Bernardi et al. (2003). E.g., D’Onofrio et al. (2008) and Nigoche-Netro et al. (2008) show that a decreases if faint galaxies are removed from the sample, and one does not account for the fact that they are missing. Donofrio et al. suggest that this may reflect the fact that luminous and faint galaxies had different formation histories. We show below that, although the latter may be true, the dependence of a on sample selection alone is not a reliable

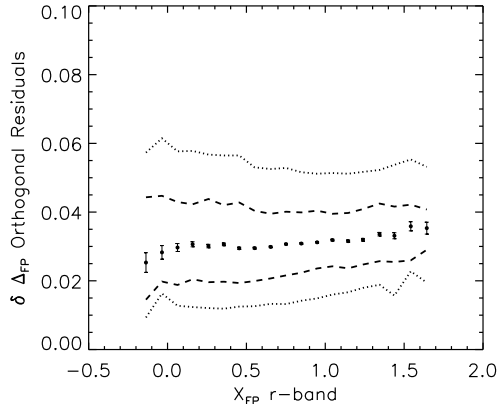


Figure 5. Contribution of measurement errors to the residuals from the orthogonal fit as a function of X_{FP} for the r -band (symbols and line styles same as previous figure). Results for other bands are similar.

indicator. We do so by constructing an FP relation using pairwise correlations with *no* curvature – so one would have concluded that nothing special was happening to galaxies at either end of the sequence. We then show that cuts in L change a and b in ways that are quite similar to that observed by D’Onofrio et al. In the following subsection, we show that similar effects also occur if cuts in σ are made.

Before discussing the FP, it is easier to first consider the size-surface brightness relation. At fixed L , $\langle \log_{10} R | \mu_e \rangle$ will be a line of slope $1/5$ with no scatter, *by definition*. Changing L moves this line to the left or right, but does not change the slope. However, because there is a correlation between R_e and L , more luminous galaxies are bigger on average, the high L galaxies only populate the large R part of their line; galaxies of lower L only populate the lower part of their line. Thus, in general, the full $\log R - \mu_e$ correlation, which is got by averaging over the full range in L , will have a different slope than $1/5$, with the difference being determined by the strength of the $\log R_e - \log L$ correlation.

Figure 6 shows this explicitly using three narrow non-overlapping bins in L . In any one bin, the slope of the relation (shown by the solid lines) is 0.2 . The slope obtained from combining two nearby bins will be slightly steeper; combining all three bins would yield an even steeper slope. This is a generic argument, but note that it also works when $\langle \log R_e | \log L \rangle$ increases linearly with $\log L$. Since the slope of the $\log R_e - \mu_e$ correlation is $1/5$ for a narrow bin in L , but something else when all L are included, the slope of the $\log R_e - \mu_e$ correlation will appear to depend on the range of L included in the sample *even though the fundamental underlying correlation is linear*. This, essentially, is the origin of the behaviour seen by D’Onofrio et al. (2008) and Nigoche-Netro et al. (2008).

To show this explicitly, the upper of the two dot-dashed lines in the Figure shows the result of averaging over the objects in the three luminosity bins shown in Figure 6: it is steeper than the relation for any one of the bins. Of course, in a magnitude limited survey, one does not simply average over all the luminosity bins. Rather, when objects with the full range of L are used, then each object is weighted

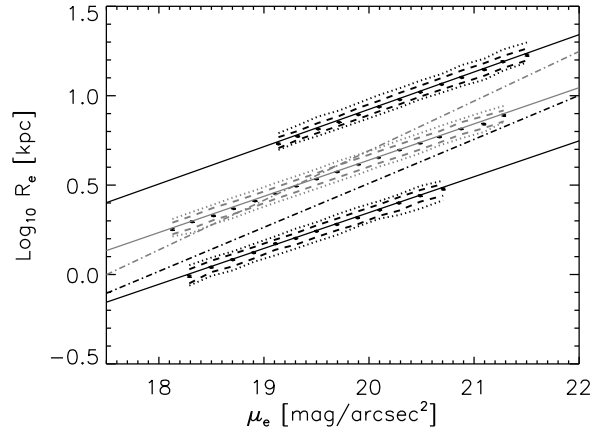


Figure 6. Effective radius versus surface-brightness in magnitude bins of (from bottom to top) $-20.5 < M_r < -20$, $-22 < M_r < -21.5$ and $-23.5 < M_r < -23$. The solid lines are linear fit to the galaxies in the different bins. The slope is 0.2 in all cases. Dashed and dotted lines show the regions which contain 68% and 95% of the objects in each bin. Upper dot-dashed curve shows a fit to the objects in all three bins, and lower dot-dashed curve shows the correlation in the full data-set which accounts for selection effect (as in Table 1 of Hyde & Bernardi 2009).

by $V_{\max}^{-1}(L)$. The lower dot-dashed line shows this relation: this shows that both the slope and the zero-point of this correlation are sensitive to this weighting.

Extending this argument to the Fundamental Plane is slightly more involved. Once again, at fixed L , the scaling between R and μ is straightforward. The inclusion of a σ -dependent term to the x-axis serves to shift the lines associated with different σ horizontally – the goal of the FP algorithm is to shift them so they lie on top of one another as much as possible. To see the effect this has, note that for a given L , each object with size R_e is shifted by an amount which depends on its σ , so the full Fundamental Plane consists of shifting each point horizontally in the $\log R_e - \mu_e$ Plane by $\langle \log \sigma | \log L, \log R_e \rangle$ on average. If the mean shift depends on R_e , this will change the slope of the line of fixed L from $1/5$ to something else. If there is scatter around this mean shift, then the line of fixed L will be broadened. The combination of change in slope and additional scatter both serve to make the parameters a and b of the Fundamental Plane depend on the range of L which are included in the fit, even though the underlying pairwise correlations are linear (i.e., their slope does not depend on L).

Figure 7 shows all this explicitly. The symbols show how the FP coefficients change as faint objects are excluded (symbols on the left) or as luminous objects are excluded (symbols on the right). Large symbols show the effect of accounting for selection effects (each object is weighted by the inverse of the volume over which it could have been observed, so luminous objects have smaller weights), and smaller symbols show results when all objects are weighted equally (selection effects are ignored). Note that a depends strongly on the luminosity cut, whereas b is less strongly affected. The smooth curves show the result of making similar measurements in a mock catalog constructed following methods given in Bernardi et al. (2003). Note in particular

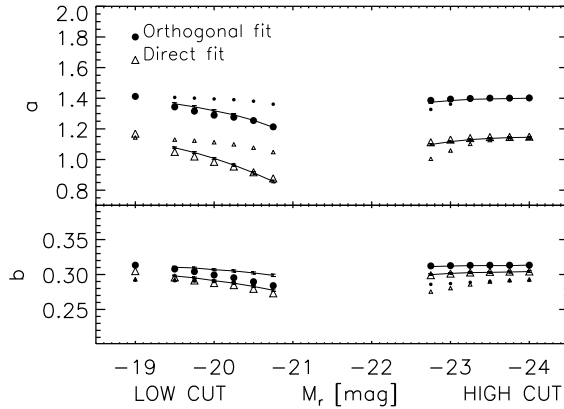


Figure 7. Dependence of FP coefficients on the luminosity range of the sample. The set of symbols on the left show how a and b change if low luminosity objects are excluded from the sample (the symbols show the absolute magnitude of the faintest object which is kept in the sample); the symbols on the right show what happens if high luminosity objects are excluded (symbols show the absolute magnitude of the brightest object in the sample). Large symbols show the result of accounting for the selection effect which comes from the apparent magnitude limit of the SDSS; smaller symbols show the result of ignoring this effect. Smooth curves show similar measurements in a mock catalog in which all underlying correlations were pure power-laws.

that all scaling relations in the mock catalog were linear; there was no curvature. Nevertheless, Figure 7 shows that the FP coefficients in the mock catalog depend on the value of the luminosity threshold similarly to how they do in the data. This demonstrates that a detection of dependence of a on luminosity threshold does *not* imply that the underlying scaling relations are curved.

The strong dependence of a on luminosity threshold is easily understood. At fixed L , R and σ are anti-correlated; it is only when averaged over a large range in L that R and σ are positively correlated (e.g. Bernardi et al. 2003). Since a is essentially the slope of the $R - \sigma$ relation, the result of restricting the range in L is to drive a to smaller values, since at fixed L it must be negative. This also explains why, when no account is taken of the magnitude limited selection, a changes little (compared to when the selection effect is accounted for) when low luminosity galaxies are excluded, but more strongly when high luminosities are excluded. In a magnitude limited sample, the luminosity distribution is biased to larger L (since they can be seen to larger volumes), so the effect of removing low L is less severe (this removes a smaller fraction of galaxies), but the effect of a cut at high L is more dramatic (this removes a larger fraction of the galaxies).

2.7 Potential biases from cuts in σ

There is no fundamental reason why we should have restricted our study to how a and b depend on L . This subsection shows how the FP coefficients change as the range of σ in the sample is varied. This study is potentially more interesting than that of the previous subsection, since few

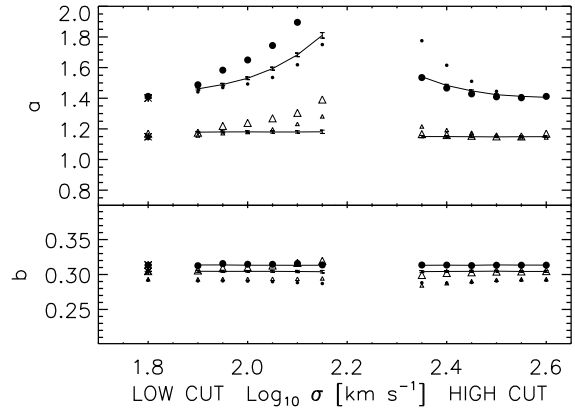


Figure 8. Dependence of FP coefficients on the range of velocity dispersions in the sample. The set of symbols on the left show measurements in samples in which objects with σ less than the value indicated were excluded; the set of symbols on the right show results when the sample excludes objects with σ larger than the indicated value. Large symbols show the result of accounting for the selection effect which comes from the apparent magnitude limit of the SDSS; smaller symbols show the result of ignoring this effect. Smooth curves show similar measurements in a mock catalog in which all underlying correlations were pure power-laws.

samples are selected on the basis of absolute magnitude, but many samples exclude objects with small σ , simply because small velocity dispersions are difficult to measure.

Figure 8 shows that b is (again) hardly affected. However, a_{orth} depends strongly on this selection, and the trend is opposite to that for luminosity, while a_{direct} is less affected (also see Bernardi et al. 2003; Nigoche-Netro et al. 2008). This is easy to understand (also see discussion in Bernardi et al. 2003): a_{direct} is close to the slope C_{RV}/C_{VV} of the $\langle \log R | \log \sigma \rangle$ relation. If this relation is linear, then excluding small or large values of σ should not change this slope. On the other hand, a_{orth} measures the orthogonal slope of this relation, and this must steepen as the bin in σ narrows; after all, in the limit of a very narrow bin in σ , this orthogonal slope must become infinite. (Sheth & Bernardi 2009 show this analytically – a_{orth} depends both on C_{RV}/C_{VV} and on C_{VV} itself. Reducing the range of σ reduces C_{VV} , thus increasing a_{orth} .) Once again, similar measurements in the pure power-law mock produce similar trends, although in this case the agreement with the SDSS is not as good. Most of this (small) discrepancy can be attributed to the fact that the underlying pairwise scaling relations in the SDSS are slightly curved (see next section), an effect which we have deliberately removed from our mocks so as to illustrate that Figures 7 and 8 are not good diagnostics of curvature.

2.8 Comparison with previous work

Our fits differ slightly from those reported by Bernardi et al. (2003). This is not unexpected, because the SDSS improved its photometric reductions significantly between DR1 (on which Bernardi et al. 2003 was based) and DR6 (on which the present analysis is based). In addition, Figure 8 shows

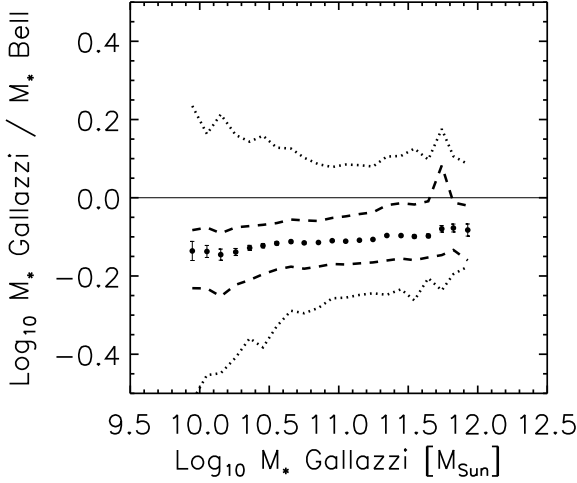


Figure 9. Comparison of the stellar mass estimates from spectra (Gallazzi et al. 2005) with those from broad-band photometry (Bell et al. 2003). Symbols and line-styles same as in Figure 4.

that simply removing $\sigma < 100 \text{ km s}^{-1}$ increases a_{orth} by about 15%. This is interesting because Bernardi et al. (2003) removed objects with $\sigma < 90 \text{ km s}^{-1}$ from their sample (due to the dispersion of the SDSS spectrograph). The distribution of velocity dispersions is relatively narrow, so this cut can have a non-negligible effect. Figure 8 shows that this might bias a high by about 10%, which is about the level of discrepancy between the Bernardi et al. (2003) FP and this work (but note that the maximum likelihood method of Bernardi et al. did try to account for the cut in σ).

While the absolute values of the best-fit coefficients have changed, the relative values have not changed significantly: both a and b increase while the intrinsic scatter decreases in the redder bands. This is true whether the fit minimizes the scatter in the $\log R_e$ direction, or in the direction orthogonal to the Plane. In addition, it is thinner at the large $\log R_e$ end. The weak but significant increase of a with wavelength is consistent with that reported by Bernardi et al. (2003) and, more recently, by La Barbera et al. (2008).

3 FP*: THE STELLAR MASS FUNDAMENTAL PLANE

The previous section studied the traditional Fundamental Plane, FP. In this section, we show the result of replacing luminosities with stellar masses to produce what we will call FP*. To illustrate that our results are robust to changes in how one estimates the stellar mass, we show results based on two different estimates of M_*/L : one, from Gallazzi et al. (2005), which is based on a likelihood analysis of the spectra; another, from Bell et al. (2003), who use the k -corrected broad-band color $(M_*/L_r) = 1.097(g-r) - 0.306$. Figure 9 compares these estimates with each other; there is an offset of about 0.15 dex and a small trend which shows that $M_{\text{Gallazzi}}/M_{\text{Bell}}$ tends to increase at larger stellar mass. Most of this offset (0.11 dex) is due to the difference in initial mass function (IMF) used in the stellar population models

Table 3. Coefficients (α, β) of the Stellar Mass Fundamental Plane. Typical uncertainties on the coefficients due to random errors are $\delta a \sim 0.02$ and $\delta b \sim 0.01$. Systematics errors give $\delta a \sim 0.05$ and $\delta b \sim 0.02$.

M_*/L	α	β	c	rms _{obs}	rms _{int}
direct					
Spectra	1.3989	0.3164	4.4858	0.1160	0.0894
Color	1.3501	0.3293	5.0015	0.1115	0.0835
orthog					
Spectra	1.6287	0.3359	4.4238	0.0648	0.0486
Color	1.5462	0.3449	4.9300	0.0638	0.0466

by the two groups. (Gallazzi et al. used Bruzual & Charlot 2003 models which assume the Chabrier 2003 IMF, while Bell et al. assume a diet-Salpeter IMF.) The rms scatter between these two estimates increases significantly at small M_* . While the offset will affect the zero-point but not the slope of the FP*, the weak trend could actually introduce a small systematic effect in the slope.

Figure 10 shows the associated Fundamental Planes, the coefficients of which are reported in Table 3. The uncertainties in δa and δb are similar to those described in Section 2.1.2 (i.e., random errors $\delta a \sim 0.02$ and $\delta b \sim 0.01$, with larger systematic uncertainties of $\delta a \sim 0.05$ and $\delta b \sim 0.02$). In this case also, understanding the errors is important. We have assumed that the error in μ_* is given by the error in the photometric quantity μ plus a contribution from the error in $\log M_*/L$. Gallazzi et al. (2005) report rms errors of about 0.06 dex, so we add 2.5 times 0.06 dex in quadrature. We further assume that the error in $\log M_*/L$ is uncorrelated with that in the size or velocity dispersion estimates. Whereas the first assumption is probably correct, the second is almost certainly incorrect for the stellar mass estimates which come from the spectra. (Gallazzi et al. 2005 do not show how the error on M_*/L correlates with the error on other observables. They do show that the M_*/L error does not correlate with spectral type.) This may explain some of the differences we see between the two stellar mass Planes.

The important point is that in both cases, the slope of FP* is steeper than that of the FP in the z -band, but it is shallower than the virial scaling. This suggests that the ratio of dynamical to stellar mass, M_{dyn}/M_* , varies systematically across the population. Our results suggest that it is a weakly increasing function of M_{dyn} or M_* . Figure 11 shows a direct comparison: $\langle M_{\text{dyn}}/M_* | M_{\text{dyn}} \rangle \propto M_{\text{dyn}}^{0.17 \pm 0.01}$ where $M_{\text{dyn}} \equiv 5R_e\sigma^2/G$ and M_* is from Gallazzi et al. (the error 0.01 on the slope was computed accounting for systematics errors – the uncertainty from random errors is smaller ~ 0.003). If there were no scatter around this relation, then we would expect $\langle M_{\text{dyn}}/M_* | M_* \rangle \propto M_*^{0.17/0.83} \propto M_*^{0.2}$; because there is scatter, this scaling is shallower, $\propto M_*^{0.06 \pm 0.01}$ (Hyde & Bernardi 2009). Gallazzi et al. (2006) also measured the M_{dyn}, M_* relationship using deVaucouleur radii of SDSS galaxies. They obtain $\langle M_{\text{dyn}}/M_* | M_{\text{dyn}} \rangle \propto M_{\text{dyn}}^{0.19 \pm 0.03}$ which is statistically equivalent to our result.

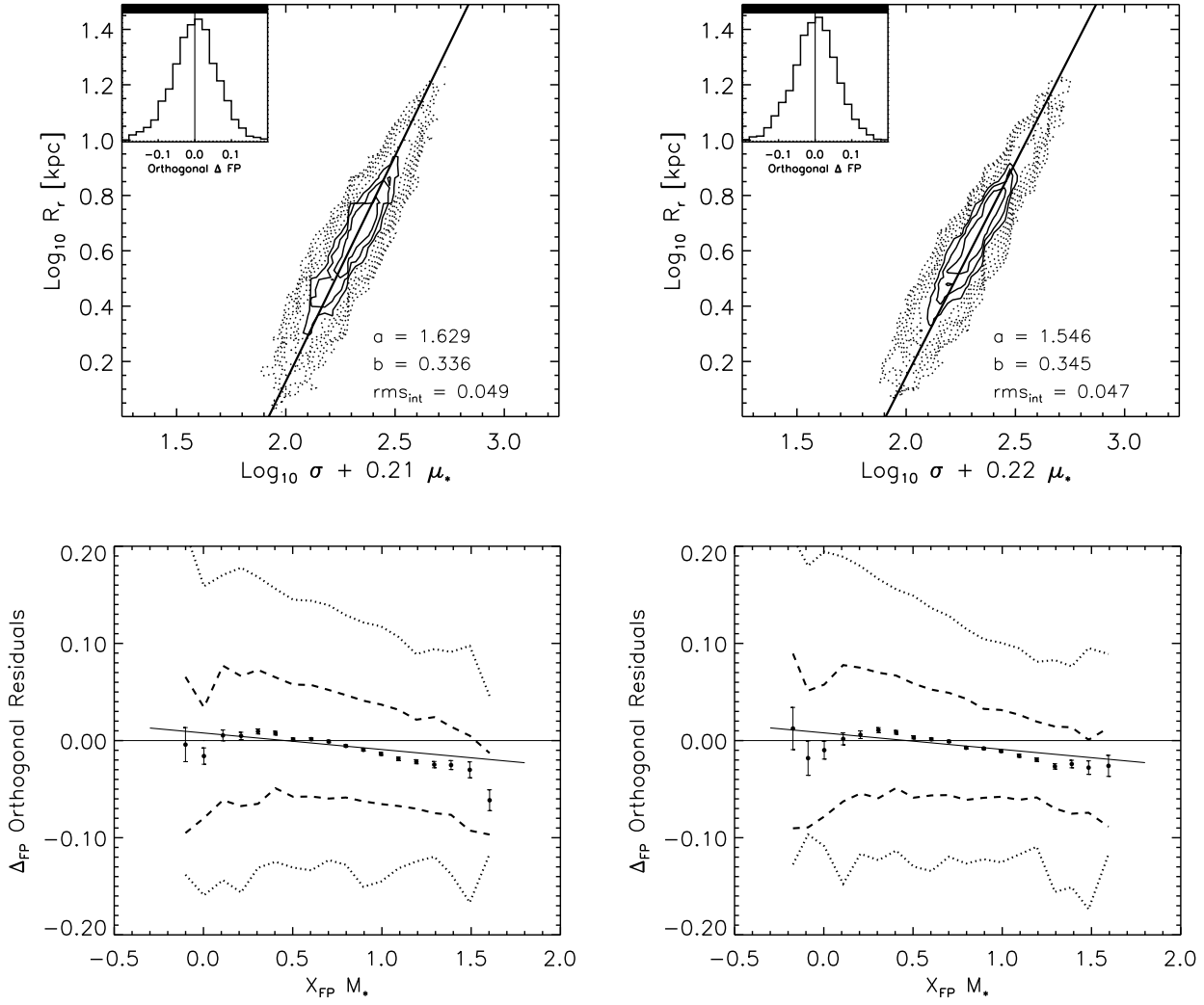


Figure 10. The stellar mass Fundamental Plane associated with the two estimates of the stellar mass (from spectra, left and photometry, right). Symbols and line-styles same as for Figures 3 and 4. Typical uncertainties on the coefficients due to random errors are $\delta a \sim 0.02$ and $\delta b \sim 0.01$. Systematics errors give $\delta a \sim 0.05$ and $\delta b \sim 0.02$.

4 THE PLANE IN κ -SPACE

Bender, Burstein & Faber (1992) suggested that the combination of variables which makes up the Fundamental Plane could be combined in a more physically transparent way. They called this combination κ -space. The three axes of this space are

$$\begin{aligned} \kappa_1 &\equiv \frac{\log_{10}(R_e \sigma^2)}{\sqrt{2}}, & \kappa_2 &\equiv \frac{\log_{10}(\sigma^2 I_e^2 / R_e)}{\sqrt{6}}, & \text{and} \\ \kappa_3 &\equiv \frac{\log_{10}(R_e \sigma^2 / L)}{\sqrt{3}}. \end{aligned} \quad (15)$$

It is interesting to examine how early types are distributed in what we call κ_* -space, which is obtained by replacing luminosity with (Gallazzi et al. 2005) stellar mass in the expressions above.

Figure 12 compares the two most interesting projections of κ_* - (left) and κ_* -space (right), when all variables have been expressed in solar units. The top panels show the ‘edge-on’

view: $M_{dyn}/L - M_{dyn}$ and $M_{dyn}/M_* - M_{dyn}$. Note that the top right panel is essentially the same as Figure 11, except that now we show the distribution using contours (objects have been weighted by $1/V_{max}$ to account for selection effects); dashed lines show forward and inverse fits, and the solid line, which has slope 0.383 and 0.429 in the two panels, shows the bisector fit.

The bottom panels show the distribution of objects within the Plane. The dashed line in the panel on the left shows $\kappa_1 + \kappa_2 = \text{constant}$ (as suggested by Bender et al. 1992). In the solar units used in the plot, the dashed line shows

$$\left(\frac{I_e}{10^{10} L_\odot / \text{kpc}^2} \right) \left(\frac{M_{dyn}/L}{M_\odot / L_\odot} \right)^{1/3} = 1.02 \left(\frac{M_{dyn}}{10^{10} M_\odot} \right)^{-1/\sqrt{3}}, \quad (16)$$

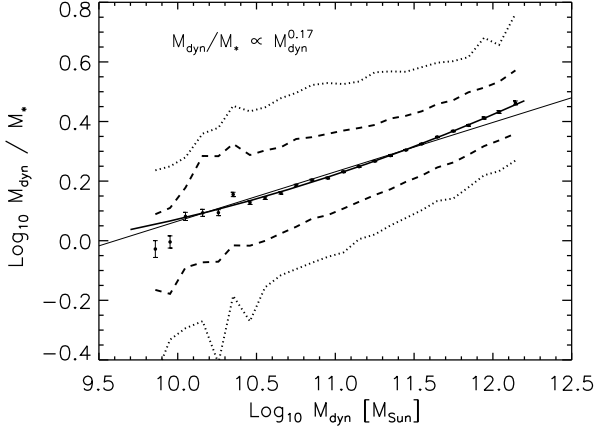


Figure 11. Ratio of dynamical and stellar masses (from Gallazzi et al. 2005) as a function of dynamical mass. Symbols and line-styles same as Figure 4. The thick solid curve is a quadratic fit (see Hyde & Bernardi 2009).

whereas it is

$$\left(\frac{M_*/R_e^2}{10^{10} M_\odot / \text{kpc}^2} \right) \left(\frac{M_{dyn}}{M_*} \right)^{1/3} = 2.04 \left(\frac{M_{dyn}}{10^{10} M_\odot} \right)^{-1/\sqrt{3}} \quad (17)$$

for the panel on the right. In the case of stellar masses, it is helpful to cube both sides of this expression, and then rearrange so that all the dependence on the dynamical mass is on the same side. This yields

$$\left(\frac{M_*/R_e^3}{10^{10} M_\odot / \text{kpc}^3} \right)^2 = 8.49 \left(\frac{M_{dyn}}{10^{10} M_\odot} \right)^{-\sqrt{3}-1}; \quad (18)$$

evidently, the dashed line expresses a relation between stellar density and dynamical mass: the upper limit to the stellar density is approximately proportional to $M_{dyn}^{-4/3}$.

5 DISCUSSION AND CONCLUSIONS

We showed that the slope of the traditional, luminosity-based Fundamental Plane FP depends weakly but systematically on waveband – it steepens towards the virial relation in the redder bands (Figure 3 and Table 2). Replacing L with stellar mass M_* leads to coefficients which are slightly closer to the virial ones; this is true whether one estimates M_*/L from the spectra or simply from broad band colors (Table 3 and Figure 10).

The stellar mass FP is slightly thinner (with an average intrinsic scatter of ~ 0.048 dex) than the luminosity-based FP (which has a typical intrinsic scatter larger than ~ 0.055 dex). The intrinsic scatter also decreases with wavelengths: from 0.062 dex in g to 0.054 dex in z .

We also showed that the intrinsic scatter around both the luminosity-based and stellar mass Planes becomes significantly broader at low sizes/masses (Figures 4 and 10) and that measurement errors account for essentially all of the observed scatter (about 0.04 dex) at large sizes/masses, suggesting that the Plane is rather thin for the very massive galaxies.

The fundamental nature of the stellar mass Plane FP_* ,

and the fact that $g-r$ color is a good indicator of M_*/L (e.g. Bell et al. 2003), explains why residuals from FP correlate with color (e.g. Bernardi et al. 2003), or, equivalently, why color may be thought of as the fourth Fundamental parameter in early-type galaxy scaling relations.

The fact that FP_* does not quite have the virial scalings suggests that the ratio of stellar to dynamical mass, M_*/M_{dyn} should vary across the population. Figure 11 showed this was indeed the case: $M_{dyn}/M_* \propto M_{dyn}^{0.17}$. This is in qualitative agreement with the results of the SAURON project (Cappellari et al. 2007), which is based on a very different analysis technique. At higher redshifts, the Fundamental Plane method is technically less challenging, so we expect it to provide a useful measure of the evolution of M_{dyn}/M_* . This will also provide a useful check on the suggestion that the slope of the correlation between M_{dyn} and M_* does not evolve out to $z \sim 1$ (Bundy et al. 2007).

We also presented an analysis of κ -space (Bender et al. 1992), but after replacing luminosities with stellar masses (using values from Gallazzi et al. 2005). The plot of M_*/M_{dyn} versus M_{dyn} referred to above is also known as the edge-on view of κ_* -space. The face-on view of the Plane in this space (Figure 12) showed that the maximum stellar density is smaller in the more massive objects: $M_*/R_e^3 \propto M_{dyn}^{-4/3}$. The κ_* -space scalings at low redshift, and an estimate of how they evolve, should provide interesting constraints on galaxy formation models.

Datasets are now sufficiently large that statistically significant curvature in most scaling relations has now been seen (e.g. Hyde & Bernardi 2009). However, illustrating that the Fundamental Plane is warped is more difficult. Previous work has shown that the coefficients of the FP can change dramatically as objects of different type (e.g. low luminosity or σ) are removed from the sample (e.g. Bernardi et al. 2003 for dependence on σ , and Donofrio et al. 2008 and Nigoche-Netro et al. 2008 for dependence on L). This has led to the suggestion that these changes indicate that the FP is warped (e.g. Donofrio et al. 2008). We showed that similar changes arise even in samples where the underlying pairwise scaling relations are not curved – i.e., when the Plane is not warped (Sections 2.6 and 2.7). Thus, the dependence of the fit parameters on the range of L or σ in the sample is not, by itself, evidence for curvature. This dependence on the range of L or σ may explain some of the relatively wide range of Fundamental Plane coefficients in the literature.

A more robust measure of how warped the Plane was also discussed. We showed that a good understanding of the errors is necessary to interpret the results; else, correlated errors might lead one to conclude there is curvature even when there is none (Figure 4 and discussion in Section 2.4). We conclude that the Plane is warped at the low size/mass end (Figures 4 and 10), and that it is also significantly broader at low sizes/masses. These conclusions are not affected by a low rate of spiral galaxy contamination, as discussed in Appendix A.

Our analysis of the bias introduced in the FP coefficients by cuts in L and σ raises an interesting puzzle. The ~ 50 objects in the SLACS sample (Bolton et al. 2008) were selected because they are gravitational lenses, meaning that they tend to have large velocity dispersions. The sample is particularly interesting because dynamic, stellar and gravitational lensing mass estimates are available. Although the

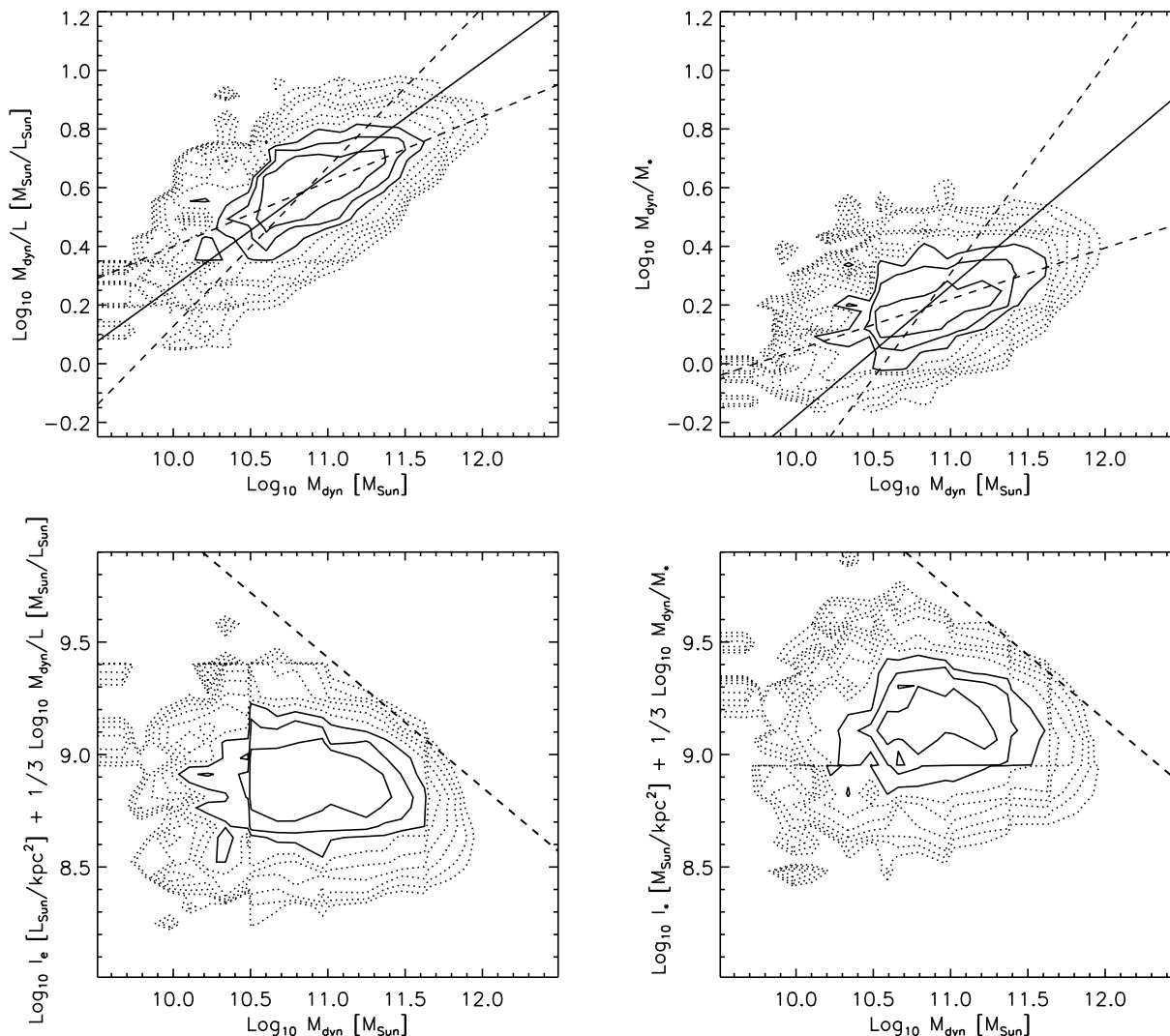


Figure 12. The κ -space Fundamental Plane in r band (left panels) and with stellar masses (from Gallazzi et al. 2005) in place of luminosity (right panels). The figure shows κ_1 , κ_2 and κ_3 transformed to solar units. Top panels show $\sqrt{3}\kappa_3$ versus $\sqrt{2}\kappa_1$; dashed lines show the direct and inverse linear fits and solid line the bisector one. Bottom panels show $\sqrt{6}\kappa_2/3$ versus $\sqrt{2}\kappa_1$. Dashed line sloping down and to right shows $\kappa_1 + \kappa_2 = \text{constant}$ scaled to solar units.

small sample size means the intrinsic thickness of the FP in this sample is almost certainly underestimated (Figure 2), what is of interest here is the fact that the smallest velocity dispersion in this sample is $\sigma \approx 160 \text{ km s}^{-1}$.

Bolton et al. make no attempt to correct for the fact that their sample has no objects with small σ . Instead, they argue that, given the same size and velocity dispersion distributions, the SLACS sample has approximately the same luminosity distribution as the parent SDSS sample from which it was drawn. They also report that the coefficients of the Fundamental Plane for their sample are rather close to the virial scalings, and they use this to motivate a number of conclusions about the origin of ‘tilt’ in most early-type samples. However, our Figure 8 suggests that if objects with $\sigma < 100 \text{ km s}^{-1}$ are missing from the sample (this is a fairly standard cut-off based on what most spectrographs used for this work are capable of), and no account is made of this,

then a_{orth} is biased high by about 15% (also see discussion in Section 2.2 as well as Figure 4 in Bernardi et al. 2003). If objects with $\sigma < 160 \text{ km s}^{-1}$ are missing, then a_{orth} is biased to values which are close to 2! Thus it is possible that the slope a_{orth} in the SLACS sample is high simply because it is biased. If so, then the conclusions about the origin of ‘tilt’ should be revised.

ACKNOWLEDGEMENTS

We thank the organizers of the meeting held in Ensenada, Mexico in March 2008 for inviting us to attend, which prompted us to complete this work. We also thank R. Sheth for helpful discussions, and A. Gallazzi for help in comparing different stellar mass estimates. J.B.H. was supported in part by a Zaccaeus Daniels fellowship. J.B.H. and M.B.

are grateful for additional support provided by NASA grant LTSA-NNG06GC19G.

Funding for the Sloan Digital Sky Survey (SDSS) and SDSS-II Archive has been provided by the Alfred P. Sloan Foundation, the Participating Institutions, the National Science Foundation, the U.S. Department of Energy, the National Aeronautics and Space Administration, the Japanese Monbukagakusho, and the Max Planck Society, and the Higher Education Funding Council for England. The SDSS Web site is <http://www.sdss.org/>.

The SDSS is managed by the Astrophysical Research Consortium (ARC) for the Participating Institutions. The Participating Institutions are the American Museum of Natural History, Astrophysical Institute Potsdam, University of Basel, University of Cambridge, Case Western Reserve University, The University of Chicago, Drexel University, Fermilab, the Institute for Advanced Study, the Japan Participation Group, The Johns Hopkins University, the Joint Institute for Nuclear Astrophysics, the Kavli Institute for Particle Astrophysics and Cosmology, the Korean Scientist Group, the Chinese Academy of Sciences (LAM-OST), Los Alamos National Laboratory, the Max-Planck-Institute for Astronomy (MPIA), the Max-Planck-Institute for Astrophysics (MPA), New Mexico State University, Ohio State University, University of Pittsburgh, University of Portsmouth, Princeton University, the United States Naval Observatory, and the University of Washington.

REFERENCES

Bell E. F., de Jong R. S., 2000, MNRAS, 312, 497
 Bell E. F., McIntosh D. H., Katz N., Weinberg M. D., 2003, ApJS, 149, 289
 Bender R., Burstein D., Faber S. M., 1992, ApJ, 399, 462
 Bernardi M., et al., 2003, AJ, 125, 1866
 Bernardi M., Sheth R. K., Nichol R. C., Schneider D. P., Brinkmann J., 2005, AJ, 129, 61
 Bernardi M., Hyde J. B., Sheth R. K., Miller C. J., Nichol R. C., 2007, AJ, 133, 1741
 Bolton A. S., Burles S., Koopmans L. V. E., Treu T., Gavazzi R., Moustakas L. A., Wayth R., Schlegel D. J., 2008, ApJ, 682, 964
 Bower R. G., Benson A. J., Malbon R., Helly J. C., Frenk C. S., Baugh C. M., Cole S., Lacey C. G., 2006, MNRAS, 370, 645
 Boylan-Kolchin M., Ma C.-P., Quataert E., 2005, MNRAS, 362, 184
 Bruzual G., Charlot S., 2003, MNRAS, 344, 1000
 Bundy K., Treu T., Ellis R. S., 2007, ApJ, 665, L5
 Cappellari M., et al., 2007, MNRAS, 379, 418
 Chabrier G., 2003, PASP, 115, 763
 De Lucia G., Springel V., White S. D. M., Croton D., Kauffmann G., 2006, MNRAS, 366, 499
 de Vaucouleurs G., 1948, AnAp, 11, 247
 Djorgovski S., Davis M., 1987, ApJ, 313, 59
 D’Onofrio M., et al., 2008, ApJ, 685, 875
 Dressler A., Lynden-Bell D., Burstein D., Davies R. L., Faber S. M., Terlevich R., Wegner G., 1987, ApJ, 313, 42
 Gallazzi A., Charlot S., Brinchmann J., White S. D. M., Tremonti C. A., 2005, MNRAS, 362, 41
 Gallazzi A., Charlot S., Brinchmann J., White S. D. M., 2006, MNRAS, 370, 1106
 Hopkins P. F., Cox T. J., Hernquist L., 2008, ApJ, 689, 17
 Hyde J. B., Bernardi M., 2009, MNRAS, 349
 Jørgensen I., Franx M., Kjaergaard P., 1996, MNRAS, 280, 167

Jørgensen, I., Chiboucas, K., Flint, K., Bergmann, M., Barr, J. & Davies, R. 2007, ApJL, 654, 179
 La Barbera F., Busarello, G. & Capaccioli, M., 2000, A&A, 362, 851
 La Barbera F., Busarello G., Merluzzi P., de la Rosa I. G., Coppola G., Haines C. P., 2008, ApJ, 689, 913
 Nelan J. E., Smith R. J., Hudson M. J., Wegner G. A., Lucey J. R., Moore S. A. W., Quinney S. J., Suntzeff N. B., 2005, ApJ, 632, 137
 Nigoche-Netro A., Ruelas-Mayorga A., Franco-Balderas A., 2009, MNRAS, 392, 1060
 Padmanabhan N., et al., 2004, NewA, 9, 329
 Pahre, M. A., Djorgovski, S. G., & de Carvalho, R. R. 1998, AJ, 116, 1591
 Robertson, B., Cox, T. J., Hernquist, L., Franx, M., Hopkins, P. F., Martini, P., & Springel, V. 2006, ApJ, 641, 21
 Saglia R. P., Colless M., Baggley G., Bertschinger E., Burstein D., Davies R. L., McMahan R. K., Wegner G., 1997, ASPC, 116, 180
 Saglia R. P., Colless M., Burstein D., Davies R. L., McMahan R. K., Wegner G., 2001, MNRAS, 324, 389
 Sersic, J.-L. 1968. “Atlas de Galaxias Australes”, (Cordoba: Obs. Astronomico)
 Sheth, R. K. & Bernardi, M. 2009, in prep.
 Thomas D., Maraston C., Bender R., Mendes de Oliveira C., 2005, ApJ, 621, 673
 Tinsley, B. M. 1978, ApJ, 222, 14
 Trager S. C., Faber S. M., Worthey G., González J. J., 2000, AJ, 120, 165
 Tremonti, C. A., et al. 2004, ApJ, 613, 898
 Worthey, G. 1994, ApJS, 95, 107

APPENDIX A: SAMPLE SELECTION AND DISK CONTAMINATION

The main text describes how our sample was selected; the main cut is on the shape of the light profile $\text{fracDev} = 1$. However, a non-negligible fraction of these objects (about 20%) have $b/a < 0.6$, which we remove because we believe the axis ratio is caused by an edge-on disk component. Presumably, similar objects viewed faced-on remain in our sample, so the question arises as to how they may have affected our results.

To address this, we divided the full sample in 5 bins in luminosity, randomly selected ~ 200 galaxies in each bin, and classified them, by eye, as E/S0, Spirals, and Others (irregulars, low surface brightness objects, interacting systems, projections). The different panels in Figure A1 show these classifications in four luminosity bins. In each panel, the solid histogram (the one with the most counts) contains ~ 200 objects (a few objects were removed because of contamination of a bright star or misclassification). The dot-dashed histogram shows the subset with $\text{fracDev} = 1$ in both g and r bands, the dashed histogram shows the result of applying all our other cuts except the one on b/a , and the dotted shows the result of excluding objects with $b/a < 0.6$. This shows that $\text{fracDev} = 1$ removes most of the Spirals and Others – our further cuts help in reducing the left over contamination.

While our selection removes most of the later type galaxies, it is perhaps surprising that a significant fraction of the objects we classified as ellipticals by eye do not have $\text{fracDev} = 1$. A selection of these objects is shown in Figure A2; it is evident that many of these objects are only

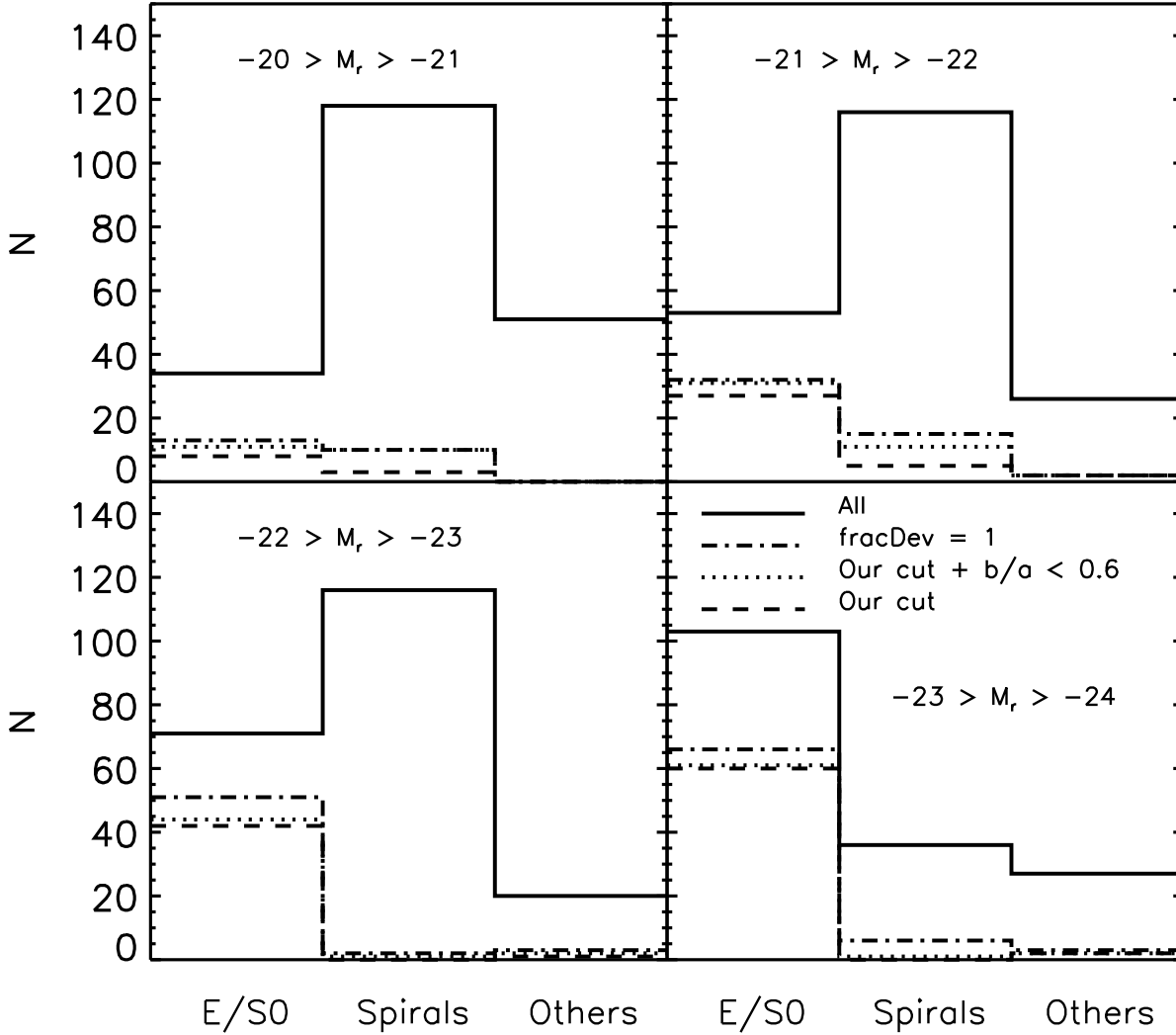


Figure A1. Effect of selection cuts on the morphological composition in our sample, shown for four bins in absolute magnitude. Solid histogram shows everything, dot-dashed is the subset with $\text{fracDev} = 1$, dotted is the smaller subset which has spectra and satisfies our cuts in eClass , and dashed is for $b/a \geq 0.6$.

marginally E/S0s, so we are confident that $\text{fracDev} = 1$ is a reliable cut. To illustrate the effect that such objects might have had on our results, the diamond-shaped symbols in Figure A3 show their location relative to the FP defined in the main text. These objects are offset to higher sizes, and they have substantially higher scatter around the FP (see inset at top left), suggesting that our decision to exclude them from the analysis in the main text, is reasonable.

The filled circles and open squares in Figure A3 show objects we classified as E/S0s and Spirals, and which satisfied our selection cuts on fracDev and b/a (i.e., they make up the dotted histogram in Figure A1). There are a handful of spirals and they tend to have larger R_e – as one might expect from trying to fit a disk component with a single deVaucouleur profile. They are a slightly larger fraction of the total counts at small $\sigma + 0.21\mu_e$, however they are so few that

they do not bias the slope, scatter, or curvature properties of the FP. Additionally, the curvature described in Section 2.4 results in negative residuals at low X_{FP} . Any curvature introduced by spiral contamination would introduce positive residuals because of artificially large radii.

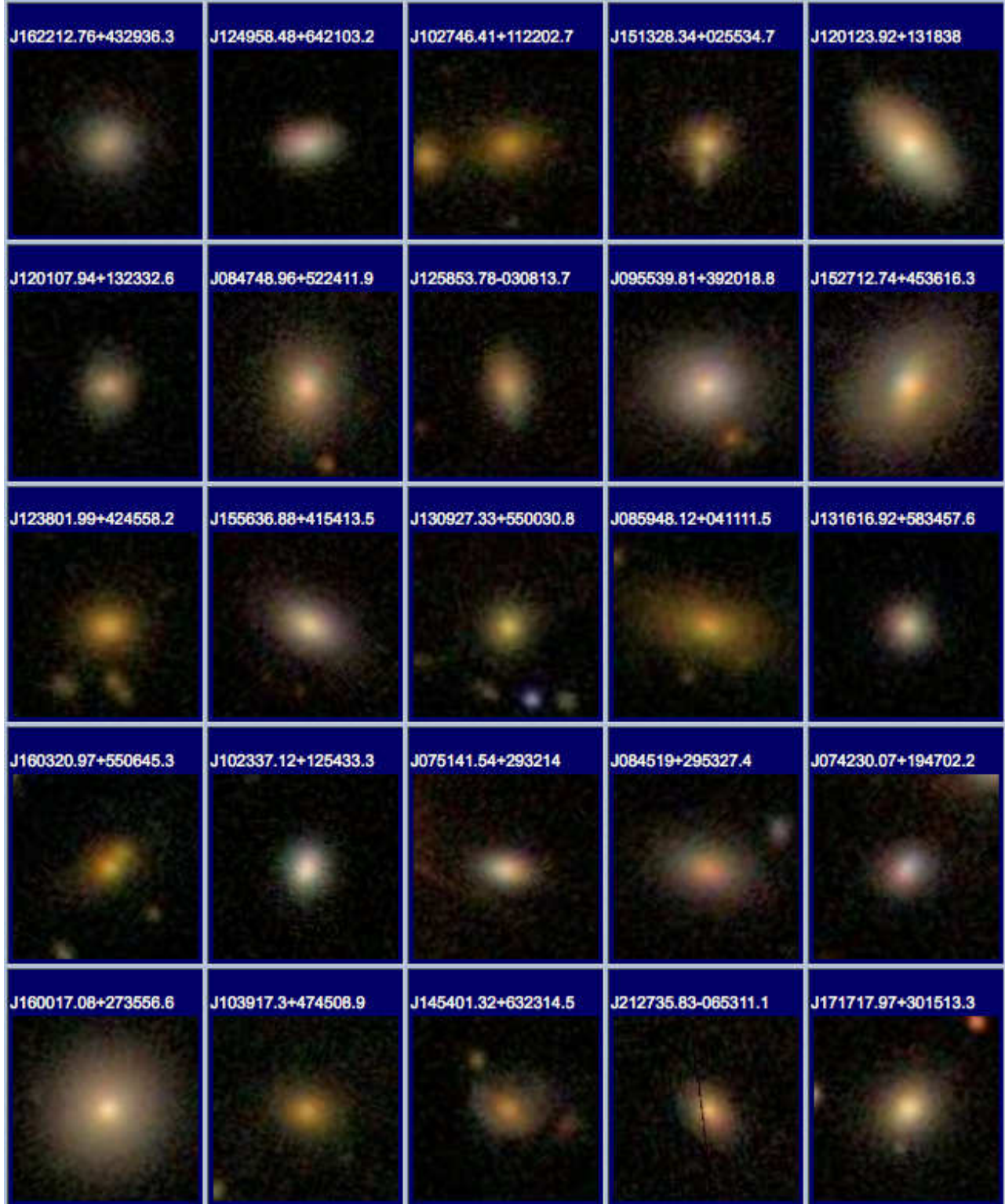


Figure A2. Selection of objects classified by eye as E/S0s, but which have $\text{fracDev} < 1$. Objects such as these are shown by the diamond symbols in Figure A3.

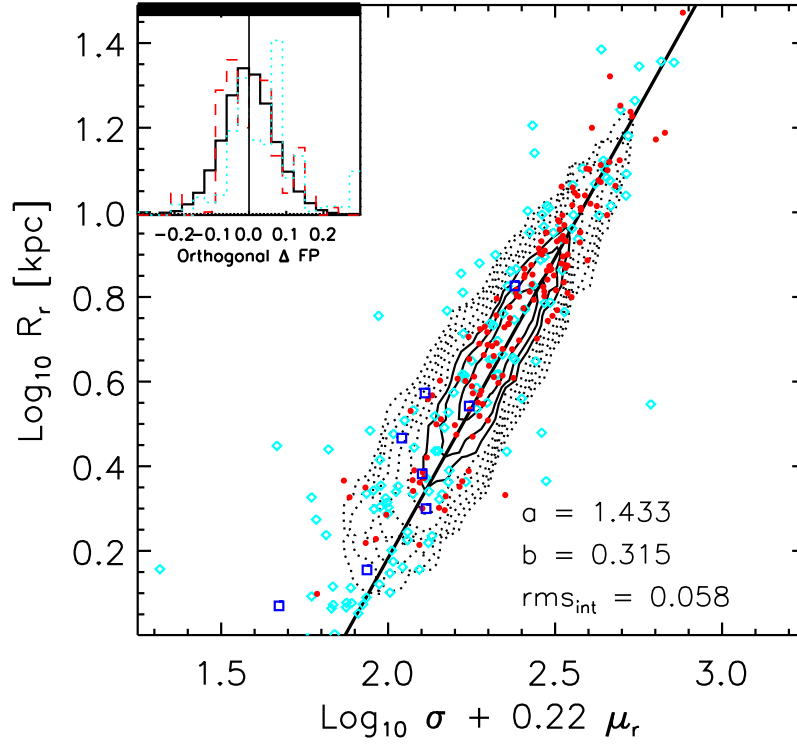


Figure A3. The Fundamental Plane in the r band (same as top right panel in Figure 3). Filled circles and open squares show objects which satisfied our selection cuts and were morphologically classified by eye as E/S0 (filled circles, see also dashed line in the inset at top left) and Spirals (open squares). Diamond-shaped symbols (and dotted line in the inset at top left) show objects we classified as E/S0 by eye but do not have `fracDev` = 1.

